The Dependence of Nadir Ocean Surface Emissivity on Wind Vector as Measured With Microwave Radiometer

Ngan Tran, Douglas Vandemark, Christopher S. Ruf, and Bertrand Chapron

***Abstract*—Global brightness temperature observations of TOPEX/Poseidon microwave radiometer (TMR) at 18, 21, and 37 GHz have been collocated with near-simultaneous SeaWinds wind vector data as well as with monthly sea surface temperature and salinity products. The combined data allow us to study the dependence of zenith-directed ocean surface emissivity, at each frequency, upon both wind speed and direction. Results show a clear two-branch wind speed dependence; weak and linear below 7 $\mathbf{m \cdot s^{-1}}$ with an increase in sensitivity above that point. The observed emissivity also depends on the angle between the wind direction and TMR's antenna polarization orientation, providing satellite confirmation of aircraft-derived results. There is little change in these wind vector dependencies with frequency.**

***Index Terms*—Nadir ocean surface emissivity, SeaWinds wind vector, TOPEX/Poseidon microwave radiometer (TMR).**

I. Introduction

The TOPEX/Poseidon microwave radiometer (TMR) is a three-frequency radiometer operating on the TOPEX/Poseidon (T/P) satellite. It measures radiometric brightness at 18, 21, and 37 GHz in a nadir-viewing direction co-aligned with T/P radar altimeters [1]. Its primary objective is to monitor and correct for the propagation path delay of the Ku-band altimeter signal due to atmospheric water vapor and cloud liquid water [2]. For TMR, this wet tropospheric path delay is derived from the three-frequency brightness temperatures T_b as discussed in [3]. Delay is highly variable in space and time and, if uncorrected, leads to altimeter range measurement errors of 3–45 cm. TMR is designed to provide this range correction with 1.2 cm accuracy.

Most satellite altimeters are now supported by a two- or three-frequency water vapor radiometer. One issue in designing these systems is compensation for the second-order brightness temperature variations associated with changing ocean surface emission. While the wind speed dependence of zenith-directed emission is fairly well known and already characterized within path delay algorithms, it has also been shown [4] that there should be a small ΔT_b associated with wind direction change. This sensitivity comes from the fact that the thermal emission from anisotropic sea waves depends upon azimuthal (polarization at nadir) observation angle.

Several experimental studies have addressed this sensitivity to the wind vector by means of circle flights [4]–[8]. These aircraft measurements indicate a direction detection capability for nadir-looking systems as well as a potential error source for spaceborne water vapor radiometers (such as TMR) aboard altimeter platforms. Reported measurements and theoretical investigations [9]–[11] suggest that the nadir-looking radiometer directional sensitivity follows from the azimuthal anisotropy of the spatial spectrum of short-gravity and capillary waves.

The aim of this communication is to use satellite data from the TMR to document the impact of wind speed and direction on surface emissivity at 18, 21, and 37 GHz. To the authors' knowledge, the study presents the first on-orbit evidence of a wind direction dependence at nadir. This work follows similar efforts focused on the off-nadir pointing spaceborne Special Sensor Microwave/Imager (SSM/I) deployed on the Defense Meteorological Satellite Program (DMSP) missions [12], [13]. The approach is simply to observe ΔT_b variation versus the angle between TMR's linear polarization alignment and the surface wind direction. To this end, a large global data set has been compiled by combining scatterometer (SeaWinds) wind vector measurements with T/P observations at satellite crossover points over a year-long period. The extensive data set carries a broad coverage of environmental conditions and permits robust removal of the first-order atmospheric signal needed to isolate the surface emission signals with certainty. In Section II, we recall Giampaolo and Ruf's [14] approach for TMR emissivity estimation using quantities that can either be obtained directly from satellite measurements or approximated from ancillary sources with satisfactory accuracy. Section III describes the large global compilation of TMR, SeaWinds wind vector, the monthly sea surface temperature (T_s) climatological estimates, and the climatological sea surface salinity (SSS) product used in this study. Sections IV and V present, respectively, wind speed and wind direction dependencies of the sea surface emissivity as measured with TMR. Section VI provides conclusions.

II. Estimation of Sea Surface Emissivity

Sea surface microwave emission for a given frequency and viewing geometry depends upon the sea water dielectric constant as well as small-scale sea surface roughness and sea foam. The latter contributions generally correlate with the local surface winds while the sea surface skin temperature and salinity control the permittivity of the medium. Radiometers provide a measurement of total brightness temperature comprised of contributions from the sea surface as well as from the atmosphere and the sensor itself. Atmospheric gases, water vapor, and liquid water all serve to attenuate the microwave emission from the ocean and the radiation from these atmospheric constituents also contributes to the detected microwave power.

In practice, atmospheric contributions can be accurately estimated by a spaceborne microwave radiometer having multiple frequencies. This is the case for TMR, an atmospheric water vapor radiometer used to correct the T/P altimeter for atmospheric path delay under clear to moderately cloudy conditions using the water vapor and cloud liquid channels, 21 GHz and 37 GHz, respectively. In addition, rain and heavy cloud conditions are routinely identified and flagged. The goal of the present study is isolation of the second-order sea surface emission signal. The operational TMR atmospheric estimates allow us to invert this sea surface emissivity knowing only the TMR brightness temperatures, the sea surface temperature, and the SSS [14].

The brightness temperature T_b observed looking down through the Earth's atmosphere is approximated by the following form of the radiative transfer equation [15]

$$T_b = T_u + T_e e^{-\tau} + T_r e^{-\tau} \tag{1}$$

where

- T_u upwelling brightness from the atmosphere;
- T_e surface flux;
- T_r reflected surface brightness from the atmosphere;
- τ opacity of the atmosphere, a measure of the radiation absorbed as it passes through the atmosphere at a given frequency.

Manuscript received April 23, 2001; revised August 26, 2001.

N. Tran and D. Vandemark are with the NASA Goddard Space Flight Center, Wallops Flight Facility, Wallops Island, VA 23337 USA (e-mail: tran@osb1.wff.nasa.gov).

C. S. Ruf is with the Department of Atmospheric, Oceanic and Space Sciences, University of Michigan, Ann Arbor, MI 48109 USA.

B. Chapron is with the Département d'Océanographie Spatiale, IFREMER, Centre de Brest, Plouzané 29280, France.

Publisher Item Identifier S 0196-2892(02)03264-3.

The surface flux is the product of the sea surface temperature T_s and surface emissivity ϵ

$$T_e = \epsilon T_s. \tag{2}$$

The reflected brightness is the fraction of the downwelling brightness T_d from the atmosphere and cold space that is reflected by the Earth's surface

$$T_r = (1 - \epsilon) T_d. \tag{3}$$

By solving the previous equations, ϵ can be expressed as a function of T_b, T_u, T_d, T_s, and τ. These terms can be obtained either from satellite measurements or derived from ancillary sources as follows. T_b is readily measured by TMR at three frequencies. Opacity for each TMR observation is estimated from the TOPEX retrieved path delay, which is itself derived from the three TMR T_b, with a simple quadratic series. T_u and T_d are approximated from the sea surface temperature by using a regression model developed by Wentz [12], [16]. More details on this solution for ϵ can be found in [14]. Note that since four unknowns (emissivity at each of three frequencies plus atmospheric opacity) are derived from three T_b measurements, this problem is underdetermined. The solution used here necessarily imposes a correlation between the errors in each of the four retrieved parameters.

Sea surface emissivity ϵ computed by this approach is generally assumed to correspond to the sum of two components [12]. The first component is the emissivity for a specular (i.e., perfectly flat) sea surface, ϵ_o. The second component is the change in emissivity $\Delta\epsilon$ due to sea surface roughness and foam. This latter component is called the wind-induced excess emissivity. It is a straightforward problem to calculate the specular ocean emissivity. It is computed from the Fresnel equation, which is a function of polarization, incidence angle, and the dielectric constant. The dielectric constant is a function of the radiation frequency, water temperature, and salinity. Expressions for the dielectric constant of saline water are given by many investigators, notably Klein and Swift [17] and Ellison *et al.* [18]. Values for this study are derived from [19], a report based on recent measurements [18], [20] over a wide range of frequencies (5–100 GHz), temperatures ($-2\ ^\circ$C–30 $^\circ$C) and salinities (22–38 parts per thousand).

III. Collocated Data Set

This study makes use of four coincident products to derive the wind-induced excess emissivity and assess its wind vector dependence: 1) TMR brightness temperatures; 2) sea surface temperature; 3) SSS; and 4) wind vector. The data used here are from four different sources. These sources are: 1) the T/P satellite mission; 2) the SeaWinds mission; 3) The Physical Oceanography Distributed Active Archive Center (PODAAC) which provides sea surface temperature; and 4) the National Oceanographic Data Center (NODC), providing the SSS.

The central collocated data set consists of a large year-long sampling of TOPEX and SeaWinds [21] crossovers as compiled by the Centre ERS d' Archivage et de Traitement (CERSAT/France). The criteria used for the collocation between these satellite crossovers are that time separation must be within 1 h and spatial separation less than 25 km between respective observations. Monthly sea surface temperature and salinity products are then added to this data set. The sea surface temperature estimates T_s come from the NCEP Reynolds optimum interpolation of monthly sea surface temperature fields on a 1° grid based on *in situ* and satellite T_s for each time period [22]. NODC provides a salinity product based on depth profiles of salinity measurements taken since 1900. A 1° grid monthly climatology for the surface salinity is used as our best estimate for the present study [23]. This approximation is assumed sufficient because the salinity impact on T_b is weak at 18–37 GHz. For our purposes both temperature and salinity data are interpolated in space to the TMR/SeaWinds measurement locations. The data set assembled for this study covers a period of about one year from July 19, 1999 to July 17, 2000. Relevant details on the two satellite products and data set filtering are provided below.

TMR flies on the T/P satellite launched in August of 1992. The satellite orbits at an altitude of 1375 km with an inclination of 66.04°. The polar orbit repeats its ground track every 9.9 days. TMR operates at 18, 21, and 37 GHz in a nadir-only viewing direction that is coaligned with the T/P radar altimeters. TMR makes use of the measurement of sea surface brightness temperature at the three frequencies: 18, 21, and 37 GHz. In addition to vapor related retrievals, this three-channel radiometer also provides valuable data related to cloud liquid abundance and, possibly, sea surface wind speed. The three channels are linearly-polarized with a common alignment. TMR does carry a second independent channel at 21 GHz with orthogonal linear polarization, but the latter serves as a back-up that has yet to be operated. TMR antenna beamwidth varies with frequency. The antenna footprint diameters on the ground are 43.4 km, 36.4 km, and 22.9 km at 18 GHz, 21 GHz, and 37 GHz, respectively. These dimensions are quite close to the scatterometer footprint insuring that equivalent spatial regions of the ocean are sampled.

The SeaWinds system on the QuikSCAT satellite represents a mission to fill the gap created by the loss of data from the NASA scatterometer NSCAT, when the ADEOS-I satellite lost power in June 1997. QuikSCAT was launched on June 19, 1999 into a sun-synchronous circular orbit with an inclination of 98.616°. The scatterometer is a microwave radar at a frequency of 13.4 GHz (Ku-band) dedicated to ocean surface wind vector measurements. The SeaWinds instrument is the first conically scanning pencil-beam scatterometer. It uses a rotating 1-m dish antenna with two pencil beams, an HH-polarized beam and a VV-polarized beam at incidence angles of 46° and 52°, respectively, that sweep in a circular pattern. The scatterometer data are sampled into 25 km × 25 km surface wind vector cells (WVC) across a 1800-km wide swath centered on the spacecraft's nadir subtrack. All backscatter measurements contained within a WVC are used to derive the WVC wind solutions. Due to the conical scanning, a WVC is generally sampled when looking forward (fore) and a second time when looking aftward (aft). Up to four measurement classes emerge: 1) HH-pol fore; 2) HH-pol aft; 3) VV-pol fore; and 4) VV-pol aft, in each WVC. However, due to the smaller swath (1400 km) viewed in HH-pol at 46° incidence, the outer swath WVCs have only VV-pol fore and aft backscatter measurements. At the swath extremes, the Earth surface is only illuminated by a single azimuth look. The limited azimuth sampling degrades wind direction estimates. Outside these special locations, the full wind vector at 10 m height can be determined accurately over a large extent of the swath. For further information on the QuikSCAT instrument and data, see the QuikSCAT user's manual [21].

In generating our final data set, both TOPEX and SeaWinds data are filtered as prescribed by each user handbook. In addition, a special correction to the 18 GHz TMR data is applied due to a documented drift in the 18 GHz channel [24]. A constant value of 1.1 K is subtracted before using this brightness temperature value. For this study, we also limit the data to low humidity and clear sky conditions. This is implemented by limiting TMR-estimated wet path delay to values below 15 cm and integrated liquid water L_z to less than 100 μm. Additionally, sea surface temperature is restricted to be greater than 2 $^\circ$C to prevent sea ice contamination. After all filtering operations, approximately 270 000 measurements remain.

Fig. 1 presents the distribution of the filtered open-ocean data. Nearly all collocated data lie in the mid-latitudes between 20° and 60°

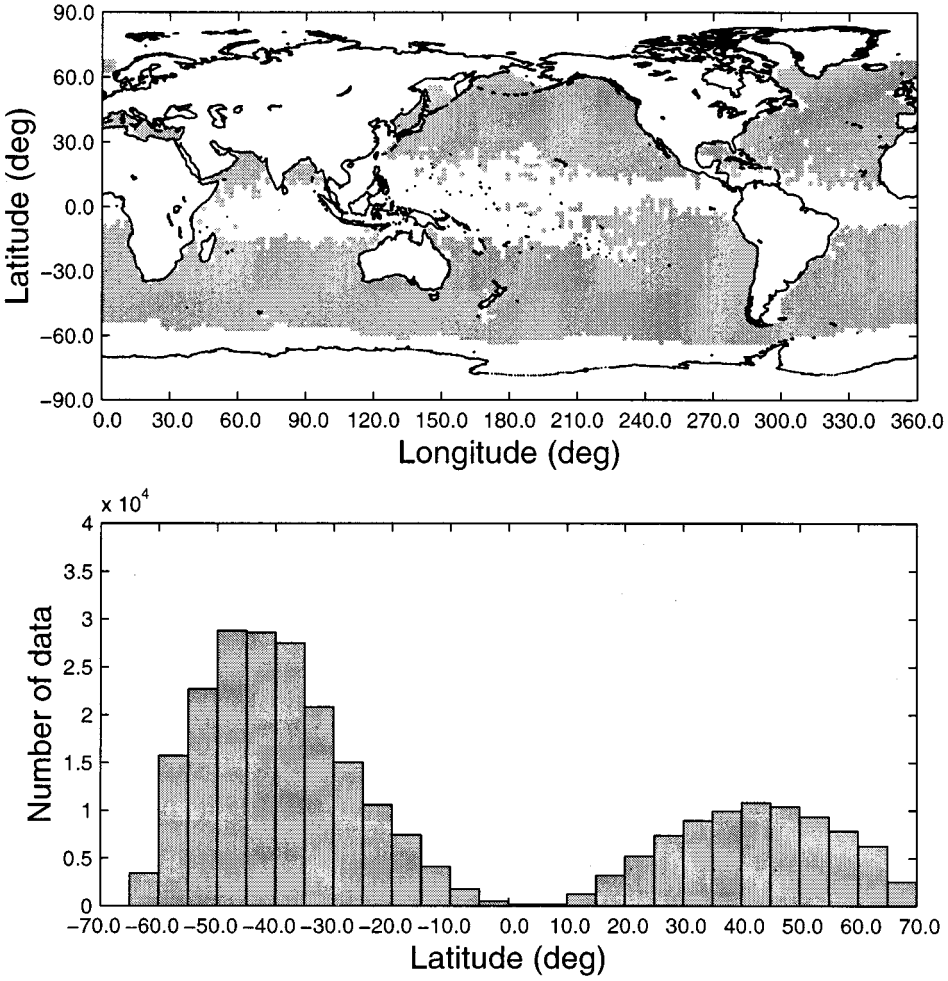

Fig. 1. Distribution of the filtered open-ocean data with respect to latitude.

TABLE I
RANGE VALUES FOR T_b AND DERIVED-VARIABLES T_u, T_d, $e^{-\tau}$, AND ϵ_o AT 18, 21, AND 37 GHz, RESPECTIVELY

		T_b (K)	T_u (K)	T_d (K)	$e^{-\tau}$	ϵ_o
18	min.	123.3	4.2	4.3	0.95	0.39
	max.	165.5	12.1	12.2	0.99	0.43
21	min.	128.6	6.3	6.4	0.87	0.39
	max.	182.0	35.0	35.2	0.98	0.45
37	min.	141.5	13.6	13.7	0.91	0.43
	max.	178.0	24.4	24.5	0.95	0.52

where dry conditions prevail. There are few data around the equator in the intertropical convergence zone (ITCZ) where water vapor is high and rain events are frequent [25].

The range of values for TMR T_b and variables discussed in Section II ($T_u, T_d, e^{-\tau}$, and ϵ_o) are presented in Table I for the three frequencies. SSS and temperature values range, respectively, from 26.9 to 39.3 psu and from 2.0 °C to 29.3 °C. Fig. 2 shows the wind speed distribution; the mean value is 7.9 m · s^{-1}, the distribution mode is near this mean and the number of samples decreases considerably at the low and high wind speed regimes. The distribution is consistent with globally-derived winds such as from the SSM/I or SeaWinds satellites.

IV. DEPENDENCE OF EMISSIVITY ON WIND SPEED

The sensitivity of TMR T_b to wind-induced emissivity is known to be small [3] compared to ΔT_b due to the atmospheric emission. Two

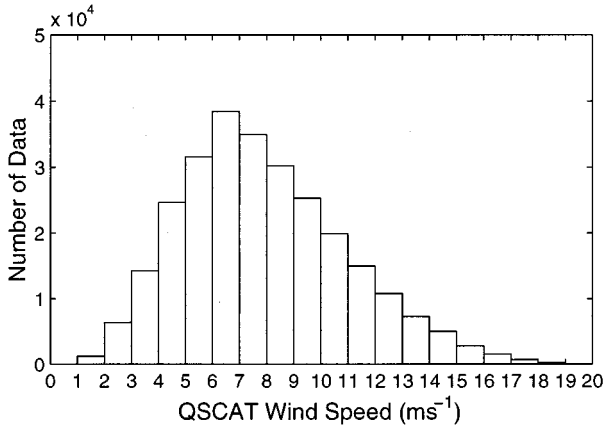

Fig. 2. SeaWinds/QSCAT wind speed distribution. The atmospheric conditions for the filtered open-ocean data are, path delay under 15 cm and integrated liquid water content under 100 μm.

filters, additional to those discussed in Section III, are used only for the wind speed sensitivity analysis of $\Delta\epsilon$. These are intended to further limit any systematic $\Delta\epsilon$ error due to possible small inaccuracies in the atmosphere model. First, the path delay limit at 18, 21, and 37 GHz is decreased from 15 to 10 cm to decrease the range of water vapor contributions and insure optimal opacity estimates [14]. Second, cloud liquid water levels are limited to less than 10 μm at 37 GHz only, where

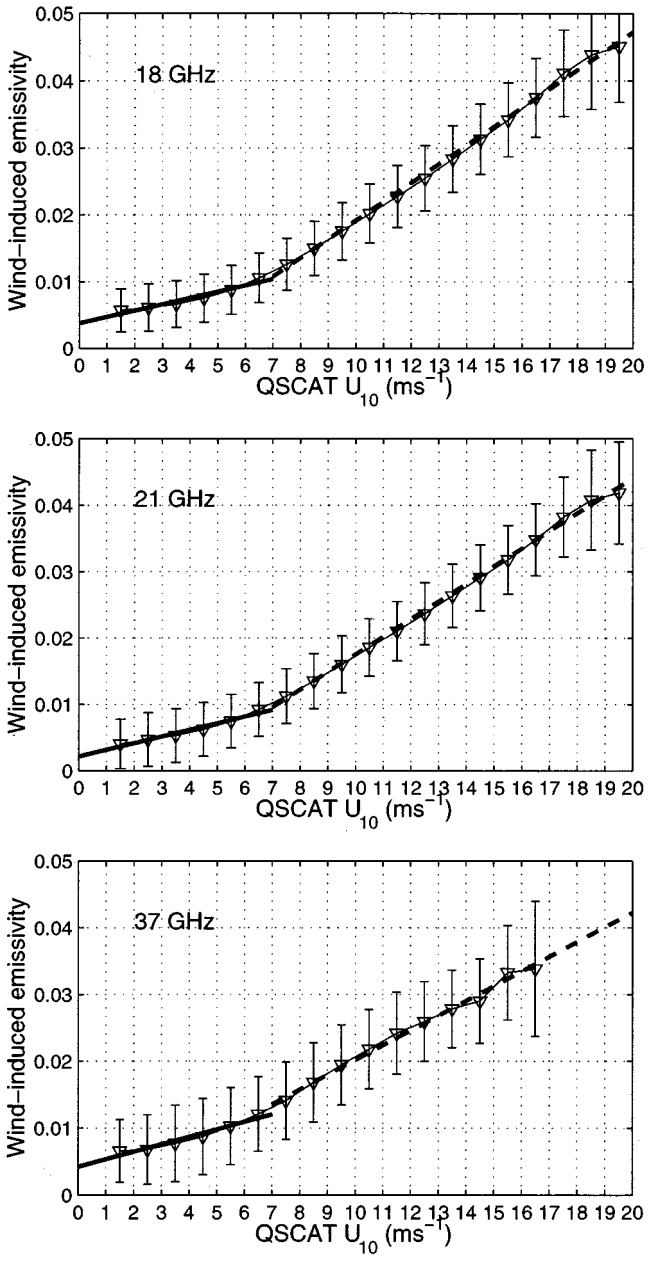

Fig. 3. Wind-induced excess emissivity at 18, 21, and 37 GHz as a function of SeaWinds/QSCAT wind speed. The atmospheric conditions: path delay under 10 cm and integrated liquid water content under 100 μm for data at 18 and 21 GHz; path delay under 10 cm and integrated liquid water content under 10 μm for data at 37 GHz. Error bars indicate ± 1 standard deviation. The lines represent least-square regression for the low and high wind speed regimes.

cloud moisture is the biggest factor. These filters reduce the number of data by $\sim 42\%$ and $\sim 58\%$ at 18 (and 21) GHz and 37 GHz, respectively.

Wind-induced emissivity values for each TMR channel are averaged against the SeaWinds wind speed using 1 m $\cdot$ s^{-1} bins, as shown in Fig. 3. These panels represent the globally-derived 18, 21, and 37 GHz nadir-view wind-induced excess emissivity as a function of scatterometer-derived 10 m wind speed. The wind speed dependence at each frequency displays the same characteristics: a clear two-branch wind speed dependence; weak and linear below 7 m $\cdot$ s^{-1} with rapid increase in sensitivity above that point. Linear regressions based on the averaged points are shown by solid lines for the wind speed range below 7 m $\cdot$ s^{-1} and by dashed lines for the wind speed range above 7 m $\cdot$ s^{-1}.

TABLE II
SLOPES OF THE LINEAR FIT AT 18, 21, AND 37 GHz IN BOTH SEAWINDS LOW (1–7 m $\cdot$ s^{-1}) AND HIGH (7–18 m $\cdot$ s^{-1}) WIND SPEED RANGES

x10^{-3}(s/m)	18 GHz	21 GHz	37 GHz
1-7 m$\cdot$s^{-1}	0.9 $\pm$ 0.3	1.0 $\pm$ 0.3	1.1 $\pm$ 0.3
7-18 m$\cdot$s^{-1}	2.8 $\pm$ 0.1	2.7 $\pm$ 0.1	2.2 $\pm$ 0.1

TABLE III
SLOPES OF THE LINEAR FIT AT 18, 21, AND 37 GHz IN BOTH TOPEX ALTIMETER LOW (1–7 m $\cdot$ s^{-1}) AND HIGH (7–18 m $\cdot$ s^{-1}) WIND SPEED RANGES

x10^{-3} (s/m)	18 GHz	21 GHz	37 GHz
1-7 m$\cdot$s^{-1}	0.6 $\pm$ 0.3	0.6 $\pm$ 0.2	0.7 $\pm$ 0.2
7-18 m$\cdot$s^{-1}	3.1 $\pm$ 0.3	2.9 $\pm$ 0.3	2.5 $\pm$ 0.4

Table II provides the regression slope values for each frequency and for both low and high wind speed regions. Considering each fit's 0.95 confidence interval, the wind sensitivity of $\Delta\epsilon$ at the three frequencies is equivalent for the low wind speed range with a slope of 0.9–1.1×10^{-3}. The high wind speed branch suggests an overall increase of more than a factor of two compared to the light wind and a slightly higher sensitivity for 18 and 21 GHz than for 37 GHz, consistent with Wentz's SSM/I model for horizontal polarization [26].

Table III presents an independent check of Table II obtained by using TOPEX altimeter-derived wind speed in place of SeaWinds scatterometer-derived wind speed. The same comments can be made for the frequency dependence of the wind speed slopes over both wind speed ranges. The slope magnitudes are a fraction lower for the low wind speed interval of TOPEX compared with the SeaWinds product and slightly higher for the high wind speed interval. Considering the 0.95 confidence intervals for the regression slope, these independent sources of wind speed lead to nearly equivalent results. The authors recommend that the results of Table II be considered the "truth" here because it is generally accepted that the altimeter-derived wind is more susceptable to sea state-related wind errors [27] and is therefore a slightly noisier and inferior product. The increased regression uncertainty levels of Table III at high winds are consistent with this view.

The sensitivity of these results to temporal collocation is addressed by computing results for the more restrictive case of a 30-min time separation. This reduces the data set size by half. Observations and wind speed slopes are unchanged for the low wind speed range aside an increase in slope fit noise by ~ 0.1 at all frequencies. For high wind speed, the slope increases, respectively, from 2.8 to 3.0, from 2.7 to 2.8, and from 2.2 to 2.5 for 18, 21, and 37 GHz. These slight increases are not surprising as the tighter collocation criterion may provide a better, though noisier (also an increase in slope fit noise by $\sim$ 0.1 for this wind speed range), rendering for the dynamic high wind region. Larger future data sets should refine these wind speed slope estimates.

The marked change in the wind speed sensitivity of emissivity at 7 m $\cdot$ s^{-1} is in agreement with previous observations [28], [29] and empirical models [12], [30], [31] for sea surface emissivity. As generally suggested, the wind affects the surface emissivity in two ways: it roughens the surface by producing small-scale waves and it leads to wave-breaking which produces foam that is a mixture of water and small air bubbles. Sufficient foam coverage and thickness leads to a higher area-averaged effective emissivity. For low wind speeds, the foam-free $\Delta\epsilon$ results strictly from changes in sea surface waves. At higher wind speeds, as waves break, the contribution from the increasing sea foam thickness and surface coverage becomes significant and is the likely cause for the increase in ΔT_b.

Note that the retrieved wind-induced emissivity does not extrapolate to zero when the wind speed reduces to zero (see Fig. 3). It is slightly

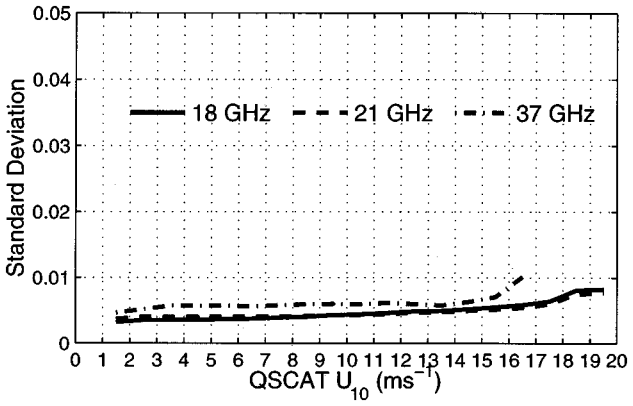

Fig. 4. Standard deviation of the wind-induced excess emissivity at 18, 21, and 37 GHz as a function of SeaWinds/QSCAT wind speed.

higher than the specular model predicts at all three frequencies by $\sim$ 0.002–0.004. There are three potential causes.

1) The Stogryn dielectric model we are using for sea water is in error. A $\sim$ 0.75% error in the model, which is well within the errors expected, would explain the behavior.
2) There is a small calibration/estimation error in our determination of emissivity due to errors in the path delay and opacity estimates along with the use of Wentz's models [12], [16] to estimate T_u and T_d. These latter models were developed using off-nadir radiometers and might introduce bias into the retrieved emissivity.
3) There exists a small residual increase in emissivity of the sea above that of a perfectly specular surface under calm wind conditions because of ever-present residual long wave swell.

Our actual bias at zero wind speed may well be a combination of all three effects.

The error bars shown in Fig. 3 indicate ± 1 standard deviation. Fig. 4 shows the standard deviation of sea surface emissivity at 18, 21, and 37 GHz as a function of SeaWinds wind speed. There is a slight increase of the standard deviation with wind speed and the 37 GHz scatter is larger than at 18 and 21 GHz. Overall, the levels are of the order of the mean $\Delta\epsilon$ values. This large signal variance suggests that wind speed may not be the sole factor influencing $\Delta\epsilon$. Both geophysical and model errors are likely contributors. Possible error in atmospheric and dielectric model components used in the $\Delta\epsilon$ inversion have been assessed at each wind speed bin. Both T_s and $\tau(T_b)$ play pivotal roles in the model but we find that systematic explained variance attributed to these terms never exceeds 20% and is usually much lower. Aside from the expected satellite crossover intercomparison and sensor estimate noise, as well as errors introduced via use of monthly T_s, there is also the possibility of systematic dependence on geophysical factors (e.g., sea state, atmospheric stability [14], [32], and wind direction) other than the wind speed itself. The averaged data represent a composite of various wind directions with respect to the observing coordinate system. Any variability related to a direction dependence contributes to the scatter.

V. Dependence of Emissivity on Wind Direction

The global data set described in Section III, with prescribed atmospheric limits, is used to assess the wind direction dependence for $\Delta\epsilon$. This relaxation of the limits from those used for wind speed evaluations leads to an average increase in the standard deviation (see Fig. 4) of $\sim$ 7% and $\sim$ 36% at 21 GHz and 37 GHz, respectively. The standard deviation at 18 GHz remains unchanged. The change is made to increase the data population and hence, directional signature estimate certainty. Implicit is the assumption that atmospheric error sources will tend to be random with respect to wind direction. The choice is also made to restrict the time threshold for pairing TMR and SeaWinds data to 30 min in order to balance the need for a large number of observations with the need for contemporaneous wind direction data from the scatterometer.

To detect possible TMR wind direction dependencies, we compute a relative wind direction ϕ, defined as the SeaWinds wind direction minus the TMR polarization direction (perpendicular to the yaw angle of the craft)

$$\phi = SeaWinds\ wind\ dir. - TMR\ polarization\ dir. \quad (4)$$

The TMR (or T/P) yaw angle defines the radiometer antenna alignment with respect to true North. Changes in T/P spacecraft yaw are frequent and designed to maintain exposure of the solar panel to the sun. When ϕ is 0° (180°), TMR polarization is parallel (anti-parallel) to the wind direction. "Crosswind" observations (in which the polarization is orthogonal to the wind direction) occur when ϕ is 90° and 270°.

Fig. 5 shows the 18, 21, and 37 GHz sea surface emissivity averaged within 20° intervals as a function of the azimuth angle ϕ for three wind speeds at ± 0.5 m $\cdot$ s^{-1}. There are clear azimuth modulations for each wind speed with a general increase in modulation strength as wind speed increases. The peak-to-peak 18 GHz $\Delta\epsilon$ directional signal increases from $\sim$ 0.0015 to $\sim$ 0.0033 for wind speeds from 7.5 to 11.5 m $\cdot$ s^{-1}. In addition, the signatures at 18, 21, and 37 GHz are similar, though data at 37 GHz are noisier than at the two other frequencies. Although this directional signal is small in comparison with the variability of the estimated wind-induced emissivity in Fig. 4 (half of the standard deviation at 18 GHz and 11.5 m $\cdot$ s^{-1}), it is clearly seen because many measurements have been averaged. TMR sea surface emissivity, observed with its linearly polarized antenna, exhibits a nearly even symmetry with respect to wind direction.

The curves of Fig. 5 represent the TMR wind direction dependence as empirically modeled by a second-order harmonic expansion which is commonly employed to model the vertically or horizontally polarized brightness temperature

$$\Delta\epsilon = a0 + a1\ cos\phi + a2\ cos2\phi. \quad (5)$$

The first harmonic $a1$ carries any upwind/downwind difference, while the second harmonic $a2$ describes the upwind/crosswind difference of sea surface emissivity. All Fourier coefficients are functions of surface wind speed and frequency.

For each wind speed range, the Fourier coefficients are obtained by least-square regression. The sea surface emissivity peaks at upwind and downwind directions and reaches a minimum at crosswind directions. This behavior is consistent with aircraft data collected at normal incidence [5], the SSM/I model function at a 53° incidence angle [12] and theoretical predictions [8], [33].

The $a0$ values derived from (5) differ only slightly from results in Table II where stricter atmospheric limits were imposed. The change occurs for the 18 and 21 GHz data in the high wind speed region and for the 37 GHz data in both the low and high wind speed regions. At 18 GHz and 21 GHz, the slope is now, respectively, 2.9×10^{-3} and 2.8×10^{-3} for the high wind speed region and at 37 GHz, the slopes become 1.7×10^{-3} and 2.4×10^{-3}, respectively, for the low and high wind speed intervals. As expected [8], there is no wind speed dependence of the first harmonic ($a1$) (results not shown). The $a1$ terms are really small and since the 95% confidence intervals for $a1$ are larger than the magnitude of the estimates of $a1$, there is no statistically significant first harmonic present in the measurements. The second harmonic ($a2$) then carries the dependence of the sea surface emissivity on the angle between the polarization plane and near-surface wind direction, as shown in Fig. 6.

Directional variation observations are nearly equal for the three TMR frequencies. Coefficient $a2$ is positive, at all frequencies for wind speed

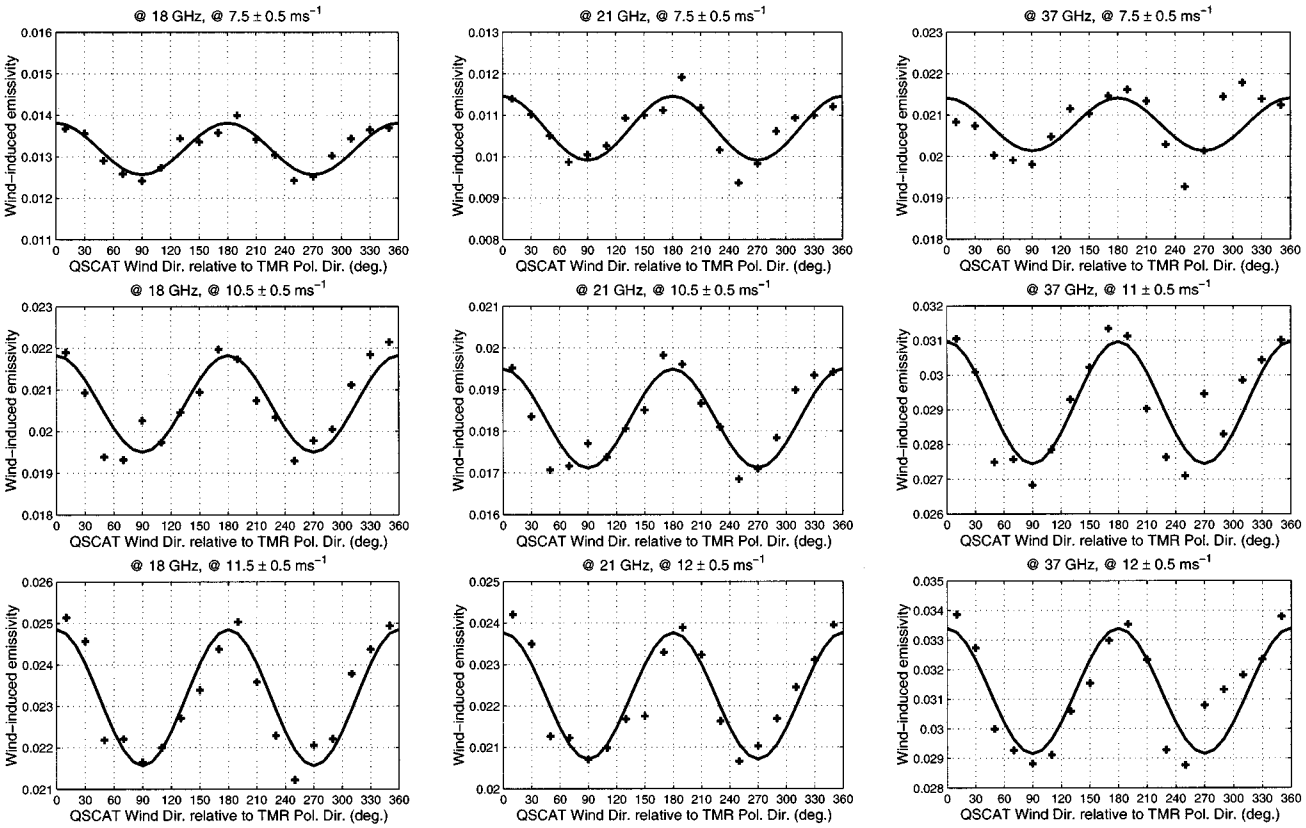

Fig. 5. Variation of wind-induced excess emissivity as a function of the azimuth angle for different wind speeds. The solid curves are second-order harmonic fits. The atmospheric conditions: path delay under 15 cm and integrated liquid water content under 100 μm for all three frequencies. The abscissa is defined in (4).

above 4 m $\cdot$ s^{-1} and the wind dependence is weak at low wind speed but increasing after 5 m $\cdot$ s^{-1}. The magnitude of 18 GHz $a2$ reaches $\sim 1.5\times10^{-3}$ at 11.5 m$\cdot$s^{-1} and seems to saturate at higher wind speed. Error bars representing the 0.95 confidence interval are larger at the highest wind speeds indicating that those results should be treated with caution. Also note that confidence intervals are larger at 37 GHz where T_b is most sensitive to integrated liquid water and T_s variations within individual directional bins. Fig. 7 shows the minimum number of data samples within the 18 20° azimuth angle bins for each 1 m $\cdot$ s^{-1} wind speed interval. This number is above 500 between 4.5 and 9.5 m $\cdot$ s^{-1}. The sizing of the bins was selected to balance the requirement for an azimuth angle bin as small as possible with the need for enough measurements to reduce the noise in individual measurements. Remaining variability may be attributed to noise in the TMR brightness temperatures, as well as errors in sea surface temperature and salinity estimations, in the wind-induced emissivity model, and in the scatterometer wind vector. Further aircraft or satellite data may serve to refine these observations, especially at high winds, but the existence of measurable azimuthal variation is certain. We note that results were also assessed using the larger data set obtained with a time window of one hour and using a larger azimuth angle bin size (30°). These changes lead to a smoother observed azimuthal variation without changing the reported $a2$ levels for light-to-moderate wind speeds. The only notable change comes for winds above 11–12 m $\cdot$ s^{-1} (not shown). Results obtained using smaller time and angular windows at high winds are likely to be more accurate, though in our case noisier, because of the dynamics within atmospheric frontal regions.

As further illustration, Fig. 8 presents the normalized second harmonic coefficient as a function of wind speed. A saturation at high winds is observed starting at about 11–12 m $\cdot$ s^{-1}. The results are similar for the three frequencies showing that the directional signal has little dependence on frequency at these frequencies. Similar saturation has been inferred from aircraft measurements at S-band and Ka-band, as summarized in [9]. The effect has also been observed for off-nadir incidence angles. The dual-frequency WINDRAD data [34] at 45, 55, and 65° incidence angles show that, in general, the azimuthal variations of brightness temperatures increase with increasing wind speed from low to moderate winds, then level off and decrease at high winds above 12 m $\cdot$ s^{-1}. As suggested, directional sensitivity of T_b at low to moderate wind speeds is likely dominated by the short wave directionality. At higher wind speeds, exceeding 12–15 m$\cdot$s^{-1}, dependence of the anisotropy on wind speed saturates or even decreases, because other factors come into play such as intense wave breaking, foam and the general change in interaction between the ocean and wind flow.

As mentioned, the TMR nadir-view directional signal changes little with frequency from 18 to 37 GHz. This is consistent with the WINDRAD aircraft data [34] at 45, 55, and 65° incidence angles and SSM/I [13].

The amplitude of the directional signal in terms of computed peak-to-peak brightness temperature is shown Fig. 9. $a2$ levels at 11.5 m $\cdot$ s^{-1} are approximately 0.4–0.5K leading to ΔT_b values of 0.8–1.1 K for 18–37 GHz. This amplitude is slightly smaller than reported H-pol data at near nadir incidence [5], [9]. [9] observed a peak-to-peak ΔT_b of $\sim$ 1.4 K for the 37 GHz horizontally polarized brightness temperature at 18° nadir viewing angle and wind speed of 10.5 m $\cdot$ s^{-1}. This corresponds to an $a2$ magnitude value of 0.6K. The observations from [5] and reported by [33, Fig. 6] show an $a2$ amplitude value of 1.0 K for 14 GHz horizontally polarized brightness temperature at a wind speed of 10 m $\cdot$ s^{-1} at 19.5 m elevation. Note that the peak-to-peak ΔT_b off nadir takes into account both $a1$ and $a2$ terms while at nadir observation ΔT_b depends only on the $a2$ term.

The slightly depressed $a2$ values in our analysis compared to previous airborne experiment results are not unexpected because the wind vector product of the scatterometer has inherent noise in the wind direc-

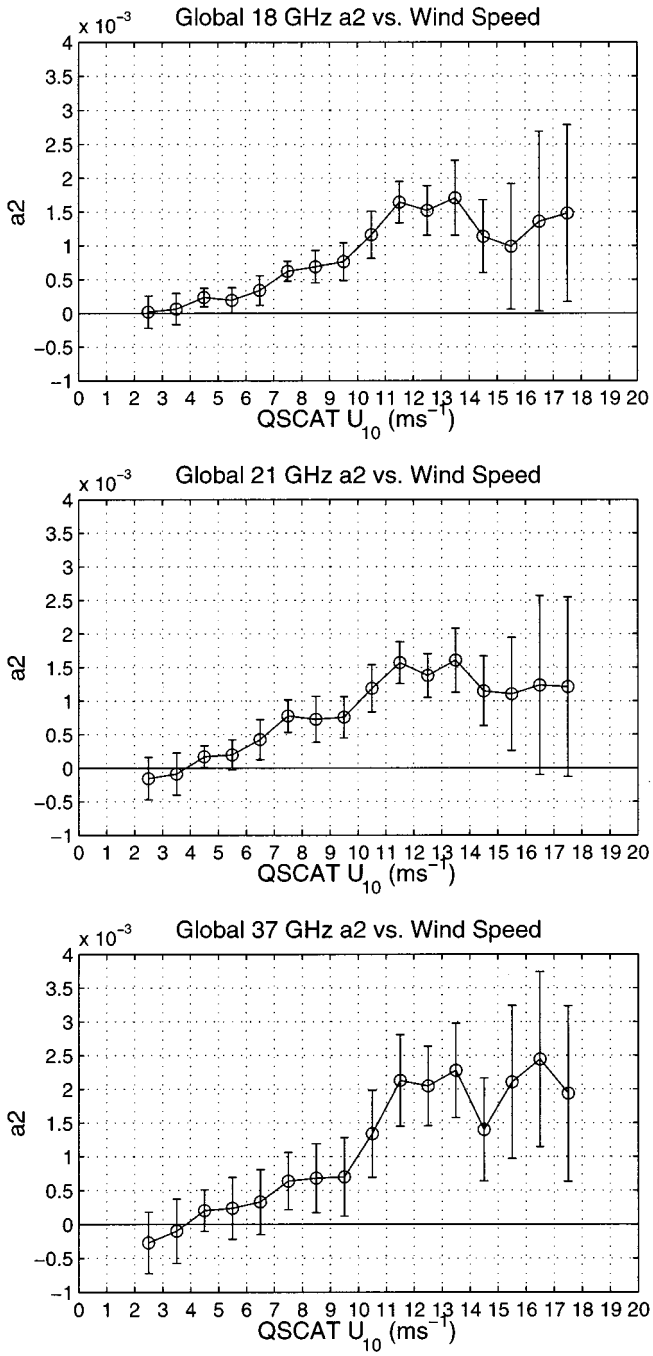

Fig. 6. Dependence of the second-order harmonic, $a2$, on SeaWinds/QSCAT wind speed. Error bars represent the 0.95 confidence interval for $a2$.

tion (of order 20%) that will degrade $a2$ sensitivity. The time window used to collocate TMR and SeaWinds crossovers may cause additional broadening leading to an underestimate of the harmonic coefficients by averaging effects. This expectation is consistent with [13]. Their results from SSM/I-ERS scatterometer matches shows a lower amplitude of the directional signal than their results based on SSM/I-moored buoys matches or those of [12] where buoys were also used.

VI. Conclusion

Observations presented in Sections IV and V serve to document the zenith-directed wind-induced ocean emissivity ($\Delta\epsilon$) at 18, 21, and 37 GHz. These data come from a carefully filtered combination of TOPEX radiometer and SeaWinds scatterometer data, augmented by

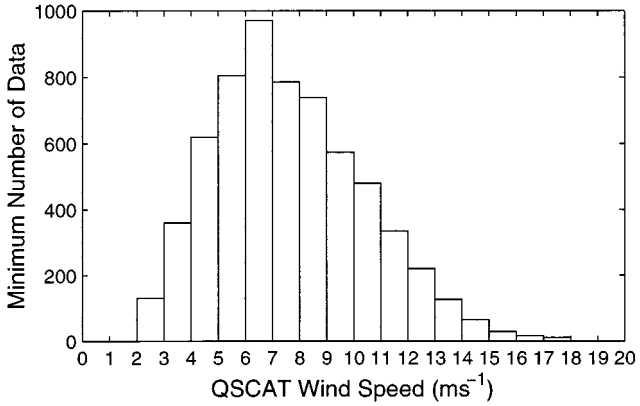

Fig. 7. Minimum number of data in a 30° azimuth angle bin for each 1 m · s^{-1} SeaWinds/QSCAT wind speed interval.

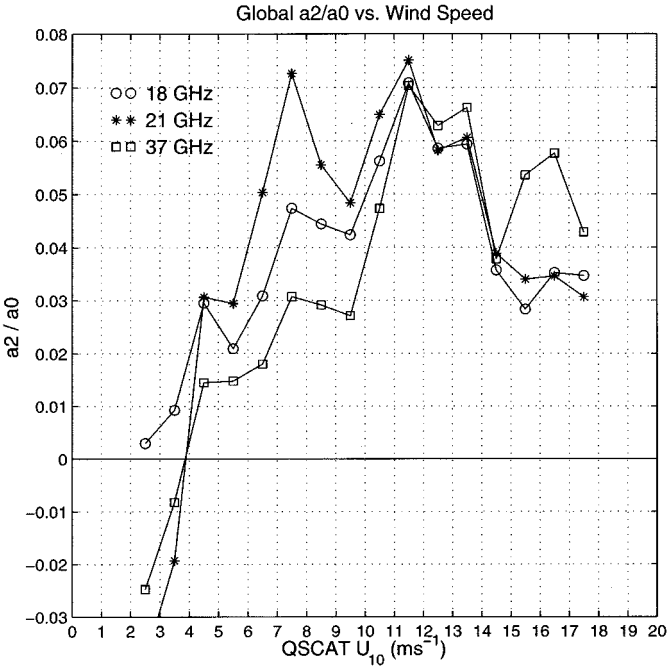

Fig. 8. Dependence of the normalized second-order harmonic $a2/a0$ on SeaWinds/QSCAT wind speed.

surface temperature and salinity estimates. The nadir-detected satellite brightness temperature is shown to depend on both wind speed and direction. This study represents the first satellite confirmation of a directional sensitivity at nadir.

The data show a clear two-branch wind speed dependence; weak and linear below 7 m · s^{-1} with an abrupt increase in sensitivity above that point for all TMR three frequencies. The $\Delta\epsilon$ is a factor of two to three higher above 7 m · s^{-1}. As mentioned, the microwave emission exhibits a smaller, but measurable, dependence on wind direction. This signal is attributed to the polarized nature of the surface wave structure. The peak-to-peak brightness temperature directional signal is of the order of 1.0 K at 11.5 m · s^{-1}. Observations vary little with frequency versus wind speed or direction. These global-average results are the product of a large data compilation and low regression uncertainties. Agreement with previous aircraft and SSM/I studies suggest high confidence in the findings.

These results are applicable in several areas. First, the data confirm the potential for a nadir-viewing wind direction sensor. Such a sensor would necessarily be a polarimetric radiometer in order to isolate the

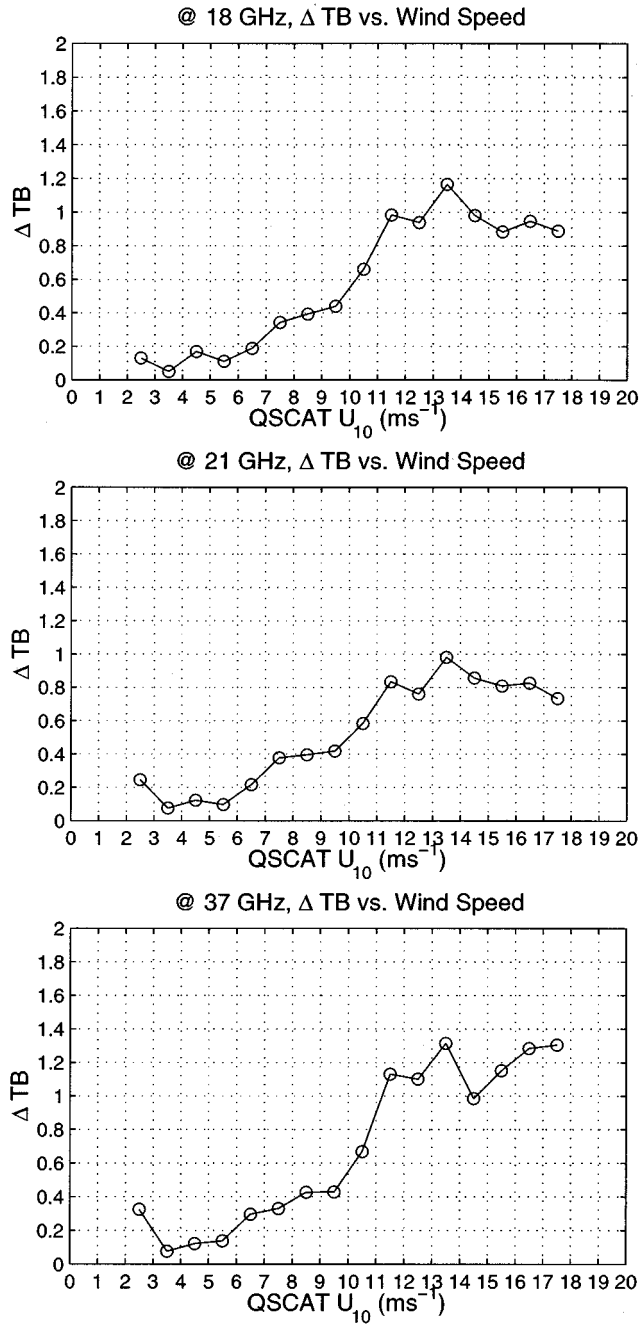

Fig. 9. Amplitude of the directional signal in term of peak-to-peak brightness temperature as a function of SeaWinds/QSCAT wind speed for the three frequencies.

polarized emission from the largely unpolarized background signal. The globally-derived observations should also serve to complement the results derived from aircraft case studies, where all measurements are being assimilated into ocean emission models [8], [34]. Finally, the accuracy of the water vapor radiometer's altimeter path delay correction can be reassessed based on the present observations. As discussed in [35], the two frequency systems are most susceptable to an additional frequency-independent error source (such as $\Delta\epsilon$ dependence on direction). For example, the GEOSAT-follow-on (GFO) or ERS radiometers operate near 22 and 37 GHz. A first-order estimate suggests that a 0.20 cm wet path delay error (and hence sea level error) will result from a peak-to-peak directional T_b variation of 1.2 K at both 22 and 37 GHz. While this level is certainly small, ocean basins can systematically differ in their mean wind directions. Therefore, the error is not necessarily random.

ACKNOWLEDGMENT

The authors wish to thank CERSAT for the TOPEX/SeaWinds collocation data set and P. Vaze at Jet Propulsion Laboratories, California Institute of Technology, Pasedena, for provision of the T/P satellite yaw data.

REFERENCES

[1] C. S. Ruf, S. J. Keihm, and M. A. Janssen, "TOPEX/Poseidon microwave radiometer (TMR): Part I—Instrument description and antenna temperature calibration," *IEEE Trans. Geosci. Remote Sensing*, vol. 33, pp. 125–137, 1995.

[2] M. A. Janssen, C. S. Ruf, and S. J. Keihm, "TOPEX/Poseidon microwave radiometer (TMR): Part II—Antenna pattern correction and brightness temperature algorithm," *IEEE Trans. Geosci. Remote Sensing*, vol. 33, pp. 138–146, 1995.

[3] S. J. Keihm, M. A. Janssen, and C. S. Ruf, "TOPEX/Poseidon microwave radiometer (TMR): Part III—Wet troposphere range correction algorithm and pre-launch error budget," *IEEE Trans. Geosci. Remote Sensing*, vol. 33, pp. 147–161, 1995.

[4] E. A. Bespalova, V. M. Veselov, V. E. Gershenzon, Y. A. Militskii, V. G. Mirovskii, I. V. Pokrovskaya, M. D. Rayev, A. G. Semin, N. K. Smirnov, V. A. Skachkov, Yu. G. Trokhimovski, Yu. B. Khapin, V. N. Chistyakov, E. A. Sharkov, and V. S. Etkin, "Surface wind velocity determination from measurements of the polarization anisotropy of microwave emission and backscatter," *Sov. J. Remote Sensing*, no. 1, pp. 121–131, 1982.

[5] M. S. Dzura, V. S. Etkin, A. S. Khrupin, M. N. Pospelov, and M. D. Raev, "Radiometers-polarimeters: Principles of design and applications for sea surface microwave emission polarimetry," in *Proc. IGARSS*, vol. 2, Houston, TX, 1992, pp. 1432–1434.

[6] Y. G. Trokhimovski, G. A. Bolotnikova, V. S. Etkin, S. I. Grechko, and A. V. Kuzmin, "The dependence of S-band sea surface brightness and temperature on wind vector at normal incidence," *IEEE Trans. Geosci. Remote Sensing*, vol. 33, pp. 1085–1088, July 1995.

[7] A. V. Kuzmin and M. N. Pospelov, "Measurements of sea surface temperature and wind vector by nadir airborne microwave instruments in Joint United States/Russia Internal Waves Remote Sensing Experiment JUSREX'92," *IEEE Trans. Geosci. Remote Sensing*, vol. 37, pp. 1907–1915, July 1999.

[8] V. G. Irisov, "Azimuthal variations of the microwave radiation from a slightly non-Gaussian sea surface," *Radio Sci.*, vol. 35, no. 1, pp. 65–82, 2000.

[9] Y. G. Trokhimovski, V. G. Irisov, E. R. Westwater, L. S. Fedor, and V. E. Leuski, "Microwave polarimetric measurements of the sea surface brightness temperature from a blimp during the coastal ocean probing experiment (COPE)," *J. Geophys. Res.*, vol. 105, pp. 6501–6516, 2000.

[10] Y. G. Trokhimovski and V. G. Irisov, "The analysis of wind exponents retrieved from microwave radar and radiometric measurements," *IEEE Trans. Geosci. Remote Sensing*, vol. 38, pp. 470–479, 2000.

[11] S. H. Yueh, R. Kwok, F. K. Li, S. V. Nghiem, W. J. Wilson, and J. A. Kong, "Polarimetric passive remote sensing of ocean wind vectors," *Radio Sci.*, vol. 29, pp. 799–814, 1994.

[12] F. J. Wentz, "Measurement of oceanic wind vector using satellite microwave radiometers," *IEEE Trans. Geosci. Remote Sensing*, vol. 30, pp. 960–972, 1992.

[13] G. A. Wick, J. J. Bates, and C. C. Gottschall, "Observational evidence of a wind direction signal in SSM/I passive microwave data," *IEEE Trans. Geosci. Remote Sensing*, vol. 38, pp. 823–837, 2000.

[14] J. C. Giampaolo and C. S. Ruf, "The effect of atmospheric stability on microwave excess emissivity due to wind," *Trans. Geosci. Remote Sensing*, vol. 39, pp. 2311–2314, Oct. 2001.

[15] N. C. Grody, "Remote sensing of atmospheric water content from satellites using microwave radiometry," *IEEE Trans. Antennas Propagat.*, vol. AP-24, pp. 155–162, 1976.

[16] F. J. Wentz, "A model function for ocean microwave brightness temperatures," *J. Geophys. Res.*, vol. 88, pp. 1892–1908, 1983.

[17] L. A. Klein and C. T. Swift, "An improved model for the dielectric constant of sea water at microwave frequencies," *IEEE Trans. Antennas Propagat.*, vol. AP-25, pp. 104–111, 1977.

[18] W. J. Ellison, A. Balana, G. Delbos, K. Lamkaouchi, L. Eymard, C. Guillou, and C. Pringent, "New permittivity measurements of seawater," *Radio Sci.*, vol. 33, pp. 639–648, 1998.
[19] A. Stogryn, "Equations for the permittivity of sea water,", Azusa, CA, Gencorp Aerojet Rep., 1997.
[20] A. Stogryn, H. Bull, K. Rubayi, and S. Iravanchy, "The microwave permittivity of sea and fresh water,", Azusa, CA, Gencorp Aerojet Report, 1995.
[21] *User's Manual for SeaWinds on QuikSCAT Science Data Products* , Jet Propulsion Labs., California Inst. Technol., Pasedena, 2000.
[22] R. W. Reynolds and T. M. Smith, "Improved global sea surface temperature analyzes using optimum interpolation," *J. Clim.*, vol. 7, pp. 929–948, 1994.
[23] M. Conkright, S. Levitus, T. O'Brien, T. Boyer, J. Antonov, and C. Stephens, "World ocean atlas 1998 CD-ROM data set documentation," NODC Int. Rep., Silver Springs, MD, Tech. Rep. 15, 1998.
[24] C. S. Ruf, "Detection of calibration drifts in spaceborne microwave radiometers using a vicarious cold reference," *IEEE Trans. Geosci. Remote Sensing*, vol. 38, pp. 44–52, Jan. 2000.
[25] G. Chen, B. Chapron, J. Tournadre, K. Katsaros, and D. Vandemark, "Global oceanic precipitation: A joint view by TOPEX and the TOPEX microwave radiometer," *J. Geophys. Res.*, vol. 102, no. C5, pp. 10 457–10 471, 1997.
[26] F. J. Wentz, "A well-calibrated ocean algorithm for special sensor microwave/imager," *J. Geophys. Res.*, vol. 102, no. C4, pp. 8703–8718, 1997.
[27] J. Gourrion, D. Vandemark, S. Bailey, and B. Chapron, "Satellite altimeter models for surface wind speed developed using ocean satellite crossovers,", IFREMER Tech. Rep. DRO/OS-00/01, 2000.
[28] G. F. Williams, "Microwave radiometry of the ocean and the possibility of marine wind velocity determination from satellite observations," *J. Geophys. Res.*, vol. 74, pp. 4591–4594, 1969.
[29] W. Nordberg, J. Conaway, D. B. Ross, and T. Wilheit, "Measurements of microwave emission from a foam-covered, wind-driven sea," *J. Atmos. Sci.*, vol. 28, pp. 429–435, 1971.
[30] T. T. Wilheit, "The effect of wind on the microwave emission from the ocean's surface at 37 GHz," *J. Geophys. Res.*, vol. 84, no. C8, pp. 4921–4926, 1979.
[31] A. T. C. Chang and T. T. Wilheit, "Remote sensing of atmospheric water vapor, liquid water, and wind speed at the ocean surface by passive microwave techniques from the Nimbus 5 satellite," *Radio Sci.*, vol. 14, pp. 793–802, 1979.
[32] M. N. Pospelov, "Surface wind speed retrieval using passive microwave polarimetry: The dependence on atmospheric stability," *IEEE Trans. Geosci. Remote Sensing*, vol. 34, pp. 1166–1171, 1996.
[33] S. H. Yueh, "Modeling of wind direction signals in polarimetric sea surface brightness temperatures," *IEEE Trans. Geosci. Remote Sensing*, vol. 35, pp. 1400–1418, 1997.
[34] S. H. Yueh, W. J. Wilson, S. J. Dinardo, and F. K. Li, "Polarimetric microwave brightness signatures of ocean wind directions," *IEEE Trans. Geosci. Remote Sensing*, vol. 37, pp. 949–959, 1999.
[35] C. S. Ruf, R. P. Dewan, and B. Subramanya, "Combined microwave radiometer and altimeter retrieval of wet path delay for the GEOSAT-follow-on," *IEEE Trans. Geosci. Remote Sensing*, vol. 34, pp. 991–999, 1996.

Low-Grazing-Angle (LGA) Sea-Spike Backscattering From Plunging Breaker Crests

James C. West

***Abstract*—The low-grazing-angle (LGA) microwave backscattering from a series of wave profiles representing the time evolution of a plunging breaker water wave is numerically calculated and compared with modeled predictions. The crest regions of the waves are isolated to remove large-scale multiple back-reflection paths that give interference. The horizontally polarized backscatter (HH) significantly exceeds that at vertical polarization (VV) during the breaking, despite the lack of multipath. Existing scattering models with some heuristic corrections are applied to the profiles to identify the dominant scattering mechanisms. The large HH-to-VV ratio is predicted from single scattering using an extended geometrical optics (EGO) approach. The initial rise in the backscatter as the wave steepens is predicted as diffraction from inflection points in the surface curvature at the crest using a modification of the geometrical theory of diffraction. The calculations show that the LGA backscattering from breaking wave crests is very complicated even in the absence of multipath and simple optically based models that treat the crest cross sections as equal at the two polarizations will be inaccurate.**

***Index Terms*—Electromagnetic scattering by rough surfaces, geometrical theory of diffraction, sea surface electromagnetic scattering.**

I. Introduction

Microwave backscatter from the sea surface is characterized by brief, strong bursts of power known as "sea spikes." At low-grazing-angle (LGA) illumination, the horizontally polarized backscatter (HH) can equal or exceed the vertically polarized backscatter (VV) during a sea spike, sometimes by greater than 10 dB. LGA sea spikes have been experimentally correlated with breaking waves, leading Trizna [1] to optically model sea spikes as multipath reflection from the the crests of breaking waves. The differing interference of the multipaths at the two polarizations can lead to the high HH-to-VV ratios observed. Using a simple representation of the wave crest, West [2] showed that the multipath scattering could indeed be predicted using optical techniques. On the other hand, when using a numerically generated time history of a plunging breaker water wave that had much more complicated crest features, Holliday *et al.* [3] found that the large HH-to-VV ratios generated were not consistent with the optically based interference models.

In this communication, the LGA scattering from the evolving crest of the plunging breaker wave train that was considered by Holliday *et al.* [3] is directly examined. The crest regions of the instantaneous wave realizations are isolated by truncating the wave immediately before and after the point of maximum height and then extending the surface to infinity at a large slope to horizontal. The backscatter is then found using a computational electromagnetic approach. By isolating the crest as described, the multipath reflection points are removed and the backscattering is entirely due to crest features. Despite the absence of multipath, the numerical calculations show that HH-to-VV ratios much greater than unity occur as the wave jet forms during breaking. Existing scattering models are then used to help isolate the mechanisms that are responsible for the calculated backscattering and to demonstrate the limitations of simple optically based models in describing the backscattering from complicated crest structures.

Manuscript received October 15, 2001. This work was supported by the U.S. Office of Naval Research Ship Structures and Systems S&T Division under Grant N00014-00-1-0082 (Program Manager Dr. R. Radlinski).

J. C. West is with the School of Electrical and Computer Engineering, Oklahoma State University, Stillwater, OK 74078 USA (e-mail: jwest@okstate.edu).

Publisher Item Identifier S 0196-2892(02)03360-0.